



Morpho-structural criteria for the identification of spreading-induced deformation processes potentially compromising stratovolcano stability

M. Rincón¹ · A. Márquez^{1,2} · R. Herrera¹ · F. Martín-González¹ · I. López¹ · C. Crespo-Martín¹

Received: 23 October 2022 / Accepted: 10 February 2023
© The Author(s) 2023

Abstract

Characterisation of surface deformation at stratovolcanoes is essential for a better understanding of the processes that can compromise edifice structural stability and potential for flank collapse. Spreading produced by the presence of a hydrothermal system or intrusion of a viscous magma body can produce similar deformation signatures, and both processes have implications for flank instability. In this work, we perform analogue models and consider examples from real volcanoes (Damavand, Ubinas, Semeru and Casita) so as to characterise and recognise surface deformation patterns produced by spreading due to the presence of a hydrothermal system and in response to magma intrusion. The experiments show that there are differences in the resulting surface deformation associated with each process. Magma intrusion results in a sharp transition between areas of subsidence and uplift, and is associated with faults with oblique strikes in the upper part of the edifice. Instead, asymmetric flank spreading is associated with hydrothermal system and results in flank bulging close to the base of the edifice. Although laboratory analogue models show different deformation responses that could be diagnostic of the associated processes, application in the field is difficult as often these diagnostic features are not preserved during evolution. However, basal bulging represents a potential diagnostic for the identification of asymmetric volcano flank spreading associated with hydrothermal activity, and the potential for instability. Remote sensing techniques can allow identification of such surface deformation features, providing a useful tool for hazard assessment and design of monitoring strategies at potentially unstable volcanoes.

Keywords Sector collapse · Deformation · Analogue models · Spreading · intrusion · Stratovolcanoes

Introduction

Catastrophic flank collapse can occur at any volcano type, independent of its composition, shape, size, or geodynamic context (McGuire 1996; Acocella 2005; Carrasco-Núñez *et al.* 2011). Emphasis has been placed on instability of catastrophic flank collapse at stratovolcanoes, especially since the eruption of Mount St. Helens in 1980, when a lateral blast occurred in conjunction with a flank collapse due to intrusion (e.g., Voight

et al. 1983; Siebert 1992; Carrasco-Núñez *et al.* 2011). Flank collapse at stratovolcanoes is a highly hazardous process that can potentially impact large areas, secondary hazards, such as tsunamis and have caused about 20,000 fatalities in historical times (Siebert *et al.* 1987). Since 1500 CE, 25 flank collapses involving a volume of material greater than 0.1 km³ have been recorded at stratovolcanoes (Carrasco-Núñez *et al.* 2011), a frequency of 4–5 events per century.

Of the 25 large historic volcano flank collapses, 16 were associated with a concomitant magmatic activity (64%), four of them were related to phreatic explosions, and in five cases no explosive component was identified (Carrasco-Núñez *et al.* 2011). The connection that exists between magma intrusion and catastrophic lateral collapse has been confirmed by discovery in the geological record of numerous examples where volcanic debris avalanche deposits contain juvenile magmatic clasts, or directly overlie nearly simultaneously emplaced eruptive deposits (Belousov *et al.* 2007; Tibaldi

Editorial responsibility: A. Tibaldi

✉ M. Rincón
marta.rincon@urjc.es

¹ ESCET, Área de Geología, Tecvolrisk Research Group, Universidad Rey Juan Carlos, Móstoles, Spain

² Departamento de Mineralogía y Petrología, Universidad Complutense, Madrid, Spain

et al. 2006). Most of the identified flank collapses, including all cases having a magmatic component (e.g., Mount. St. Helens in 1980; Voight *et al.* 1983), many cases are associated with debris avalanche deposits with no magmatic component or eruptive deposit. This includes the collapses of Mombacho (Nicaragua) in 1540 CE and Unzen (Japan) in 1792 CE (van Wyk de Vries and Francis 1997; Siebert *et al.* 1987). The prime factors for edifice instability triggering collapse without a magmatic component have been related to processes such as (1) the action of faults underlying the edifice (Lagmay *et al.* 2000; Tibaldi *et al.* 2008), (2) volcano spreading over a weak basal layer (Borgia *et al.* 1992; Borgia and van Wyk de Vries 2003), and (3) the presence of a body of hydrothermally altered rocks inside the edifice (van Wyk de Vries *et al.* 2000).

Hydrothermal alteration plays a key role as a mechanism for stratovolcano instability and lateral catastrophic collapses. This has been revealed by, first, the presence of hydrothermally altered materials in several volcanic debris avalanche deposits (e.g., Pevear 1982; Voight *et al.* 2002; Salaün *et al.* 2011); and, second, association of hydrothermal explosions with historical examples of flank collapse (Reid *et al.* 2001). For example, at Bandai volcano (Japan) in 1888 CE, a series of phreatic explosions (up to 20 per minute) occurred before the final event triggered collapse of the volcano's northern flank (Sekiya and Kikuchi, 1890). The high number of stratovolcanoes with surficial evidence of active hydrothermal systems (e.g., presence of hot springs and/or soil and fumarolic gas emissions, hydrothermally altered zones) makes it very important to study the role that hydrothermal alteration could play in triggering collapse-related hazards (Takahashi *et al.* 2018; Darmawan *et al.* 2020; Matsunaga *et al.* 2020).

The role of hydrothermal alteration in creating an edifice instability is manifold. Alteration of volcanic rocks, for example, can reduce their porosity and permeability (Berger and Henley 2011; Horwell *et al.* 2013), potentially promoting the development of high pore fluid pressures, which favours fracturing and loss of strength (Lopez and Williams 1993; Day 1996; Reid 2004; Heap *et al.* 2021). Hydrothermally altered rocks are also mechanically weaker than fresh, unaltered rocks due to the development of secondary minerals (mainly clay minerals), which have lower strength, reducing the cohesion and friction values of the rock mass (Darmawan *et al.* 2020). In addition, clay-rich altered rocks have a tendency to deform mainly by ductile mechanisms. As a result, formation of a weak and ductile body of hydrothermally altered rocks helps promote gradual spreading of the edifice (van Wyk de Vries *et al.* 2000; Cecchi *et al.* 2004). Ductile behaviour of the altered body is associated with a low deformation rate (van Wyk de Vries *et al.* 2000), making it difficult to detect geodetic monitoring technique, such as those applied to data from Interferometric Synthetic Aperture Radar (InSAR) or Global Positioning System (GNSS).

To date, the study of edifice instability in response to the formation of hydrothermally altered cores has been based on field observations (Rosas-Carbajal *et al.* 2016), remote sensing (Michon and Saint-Ange, 2008), rock mechanics (Zimbelman *et al.* 2003), numerical modelling (Kelfoun *et al.* 2021), and analogue modelling (Cecchi *et al.* 2004; van Wyk de Vries *et al.* 2000; Andrade and van Wyk de Vries 2010; Rincón *et al.* 2015; Rincón *et al.* 2018). Previous analogue modelling studies have shown that the development of a concave–convex-shaped flank can be considered a diagnostic feature of gradual asymmetric gravitational deformation in weak-cored edifices (Cecchi *et al.* 2004). As a result, the existence of concave–convex topographic profiles has been proposed as evidence for a flank spreading as, for example, at Semeru volcano, Indonesia (Solikhin *et al.* 2012). However, analogue modelling, as well as observations of historical events, such as at Bezymianny (Kamchatka) in 1959 and at St. Helens (USA), in 1980, have shown that cryptodome intrusion can also produce flank bulging result a concave–convex topographic profile (Donnadieu *et al.* 2003, Cecchi *et al.* 2004). These deformation features can be preserved for some time, even after the cessation of intrusion, and can be misinterpreted as active spreading (van Wyk de Vries *et al.* 2018). That is, an old intrusion can potentially influence the shape of the volcano for a long time, with the shape strongly resembling the morphology of an edifice that is undergoing an active spreading (Donnadieu *et al.* 2003).

Here, we present the results of analogue modelling of volcano deformation in response to the presence of a weak core and viscous magma intrusion ($\sim 1 \times 10^9$ Pa·s). The results of our experimental study inform on the deformation mechanism responsible for flank bulging, and constrain for diagnostic criteria for instabilities produced by hydrothermal activity and intrusion, as based on edifice morphology and deformation structures apparent at the surface.

Experimental methodology

Experimental setup

Two analogue model scenarios were investigated: (1) H-type intended to recreate a spreading due to the existence of a hydrothermally weak core and (2) I-type which recreates cryptodome induced instability (i.e., due to viscous magma intrusion). A mixture of fine-grained sand (80%) and plaster (20%) was used to simulate the fresh rock of the volcanic edifice for both models (cf. Rincón 2019). Such granular material is commonly used to model deformation of volcanic rocks and to visualise brittle faulting (e.g., Merle and Borgia 1996; Delcamp *et al.* 2008; Rincón *et al.* 2015; Rincón *et al.* 2018). In both setups, the cones were constructed by pouring the sand from a jar onto a rigid base above a 1-cm-thick layer of the same material as the

cone. This avoid friction between the deformable (sand) cone and the underlying (rigid) surface (Fig. 1).

In the first setup (H-type), we simulated the mechanical properties of the hydrothermally altered rocks within the volcano core with silicon (Bluesil GUM FB, PDMS) (Rincón 2018). Following Cecchi et al. (2004), we simulate hydrothermal systems developing within and below the edifice. To simulate this, the hydrothermal system was placed experiments at the base of the cone. This was the case for 12 experiments (experiments H1, H3, H4, H6, H7, H9, H10, H12, H13, H15, H16, and H18 of Fig. 2). For five experiments middle-centred, the silicone was placed within the edifice 5.5 cm from the cone base (experiments H2, H5, H11, H14, and H17 of Fig. 2).

Due to the diversity of possible shapes, sizes, and locations of the hydrothermally altered body inside a stratovolcano, we designed our experiment settings to recreate spreading caused by the presence of a hydrothermal core with different characteristics. We considered three different variables: (1) core shape: cube, prism, and cone; (2) core size: large (10% of the cone volume) and small (5%); and (3) core position: base-centre, middle-centre, and base-side (Fig. 2). The combination of these three variables resulted in 17 possible experimental settings that reproduced 17 possible scenarios for the H-type model (Fig. 2). To validate the reproducibility of these H-type experiments, experiment S6 was repeated nine times. Variability observed in cone morphology and faulting due to deformation

Fig. 1 Experimental setup. (A) H-type volcano spreading by hydrothermal core and (B) I-type cryptodome intrusion. A tripod with the Kinect sensor attached is located at a height of 0.75 m above the table. The data obtained by the Kinect sensor is sent in real time to the acquisition

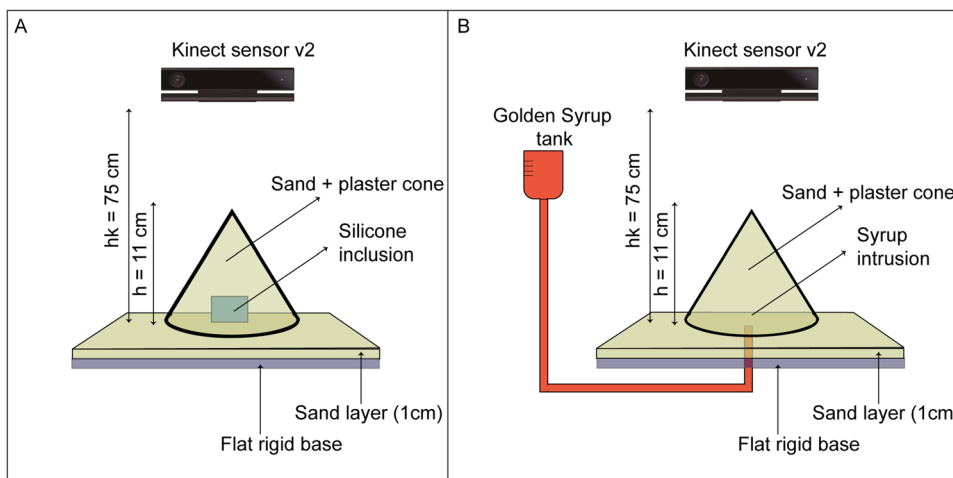
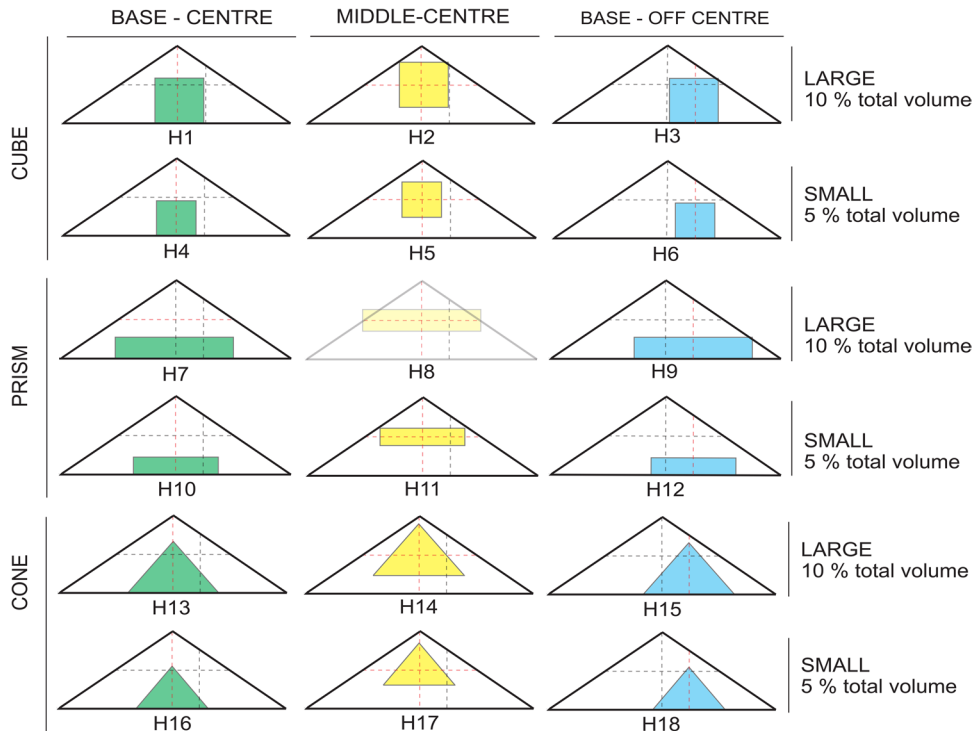


Fig. 2 Sketches of the experiments involving the combination of simulated hydrothermal system parameters (shape, size, and location). The combination resulting for experiment HEXPERIMEN8 (in red) is logistically impossible



was minimal and the same diagnostic features appeared in all nine tests (Online Resource 1). Our I-type experiment reproduces magmatic intrusion using syrup injected into the base of the cone following the methodology of Rincón et al. (2018; Fig. 1). We conducted a set of six experiments, where the only variable was the distance between the intrusion and the central axis of the cone. Experiments with distances less than 0.5 cm and distances between 1.5 and 3 cm are considered here, and results are similar to those of Rincón et al. (2018). We use a Microsoft® Kinect v2 sensor to track surface deformation and to quantify changes in the analogue model topography (Tortini et al. 2014) (Fig. 1). Microsoft® Kinect v2 combines an optical camera and an infrared distance measurement sensor. The precision of the device has been quantified by Rincón et al. (2022) and is ~ 1 mm.

Scaling and materials

To compare surface changes and fault patterns produced by the analogue models with field data for natural systems, scaling of the experiments needs to be geometrically, dynamically, and kinetically defined (Hubbert 1937). For scaling, the range of parameters considered are the same as those used by Rincón et al. (2018). For both cases, length scale $[L]^*$ is 10^{-4} (i.e., 10 m in the natural system 1 mm in the model), and cone height (hM) is 11 cm, so that a 1100-m high edifice is considered (hN). The cohesion of the material used for the model (σ_M) was estimated using a shear-ring test at the HelTec Lab of GeoForschungsZentrum (GFZ)—Helmholtz-Zentrum Potsdam, Germany (Samaniego et al. 2015). This gave values of 50–100 Pa, which simulate a fresh rock mass with a cohesion (σ_N) of $9 \times 10^5 - 2 \times 10^6$ Pa ($\approx 1-2$ MPa) (Seisdedos et al. 2012).

To simulate the hydrothermally zone, we used Rhodorsil GUM FB® silicone because of the tendency of hydrothermally altered rocks to deform mainly by creep (van Wyk de Vries et al. 2000; Cecchi et al. 2004). The viscosity of Rhodorsil FB® silicone is 1×10^4 Pa·s (Calvin et al. 2013), whereas the

viscosity of the hydrothermal core in a natural system has been estimated to be around 1×10^{18} Pa·s (van Wyk de Vries and Matela 1998). This means that one minute of a H-type experiment corresponds to around 10,000 years for the natural system. In our I-type experiments, we used Lylle's Golden Syrup TM to simulate intrusion of magma with a viscosity of around 1×10^9 Pa·s, as proposed for the cryptodome of Mt. St. Helens in 1980 (Pinkerton and Stevenson 1992). According to scaling (Table 1), our model fluxes into the intrusion (Q_m) are ~ 2 cm³/s, and scale to a value for the natural system (Q_n) of ~ 30 m³/s, which is similar to that for the Mt. St Helens cryptodome intrusion in 1980, i.e., 30 m³/s (Moore and Albee 1981).

Data analysis

Experiments were recorded monitored using the visible and distance images obtained by Microsoft®'s Kinect v2 sensor (Rincón et al. 2022). We used the visible images to map deformation structures (faults), and the distance images to quantify topographic changes. Spatial resolutions were 1920×1080 pixels for visible images and 512×420 pixels for the distance images. Since we recorded data from a height of 75 cm, pixel sizes are 0.6 mm and 1.6 mm, respectively. Temporal resolution was 1 image per second recorded, every 10 min during H-type experiments, and 1 image per second until the syrup reached the surface for I-type experiments.

To obtain quantitative values for surface deformation (e.g., degree of subsidence and/or uplift) of the cone during the experiments, we calculated the difference between the sequential distance images and a reference image, i.e., the first image acquired at the of the start of the experiment at time. For H-type experiments, we analysed images acquired after one of the minutes one (t1), two (t2), and three (t3). This, following our scaling, correspond approximately to 10,000, 20,000, and 30,000 years in a naturel system. The selected times for I-type were five (t5), 10 (t10), and 20 (t20) minutes, representing 6, 12, 19, and 25 days in the natural system.

Table 1 Scaling: Geometrical and mechanical parameter scaling and their values in the natural and modelled systems

Parameters	Definition	Model (M)	Nature (N)	Ratio (M/N)	Units (IS)	Dimensions
h	Stratovolcano height	0.11	1100	1×10^{-4}	M	[L]
R	Stratovolcano radius	0.15	15,000	1×10^{-5}	M	[L]
g	Gravity	1	1	1	$m \times s^{-2}$	[LT ⁻²]
ρ_v	Stratovolcano density	1320	2500	5.5×10^{-1}	$kg \ m^{-3}$	[M \times L ⁻³]
σ_v	Stratovolcano cohesion	50–100	9×10^5	2.5×10^{-6}	$kg \times m^{-1}$	[M \times L ⁻¹]
Φ	Friction angle	36–37	36–37	1	°	-
ts	Deformation time spreading	0–600	$0-3.2 \times 10^{12}$	$0-1.9 \times 10^{-10}$	S	[T]
ti	Deformation time intrusion	0–1.200	$0-2.2 \times 10^6$	$0-5.5 \times 10^{-4}$	S	[T]
μ_{sh}	Hydrothermal core viscosity	1×10^4	1×10^{18}	1×10^{-15}	$kg \times m^{-1} \times s^{-2}$	[M \times L ⁻¹ \times T ⁻²]
μ_m	Magma viscosity	30	1.5×10^9	3.3×10^{-9}	$kg \times m^{-1} \times s^{-2}$	[M \times L ⁻¹ \times T ⁻²]
Q_m	Magma flow	1.7×10^9	1–100	1.5×10^9	$m^{-3} \times s$	[L ⁻³ \times T ⁻¹]

Results from analogue models

Deformation by spreading due to a hydrothermally weak core (H-type models)

Most of the H-type models show visible deformation at the cone surface, both as topographic displacements and faulting (Fig. 3). The larger and closer to the surface the weak core simulating the body of hydrothermally altered rocks body is, the greater and more intense is the surface deformation (Fig. 3). The changes in surface morphology that are detected are mainly characterised by subsidence of the summit area (by up to 15 mm), so as to develop a characteristic flat (i.e., low slope) area at the summit (Figs. 3 and 4). In several experiments, this subsidence was accompanied by a surrounding zone of small positive of ~10 mm displacement. For most cases where the weak body is central to the cone interior, the faulting pattern is symmetrical, with the development of two main curved normal faults, bounding the subsidence zone, and dipping towards the centre of the cone to form a summit graben (see experiments H1, H2, H10, H11, H14, and H17 of Fig. 3). However, deformation around the flat summit area has a degree of asymmetry (see experiments H1, H2, H10, H11, H14, and H17 of Fig. 3). Experiments where the weak core was located off-centre within in the cone, the faulting pattern changes. For such cases, an early principal curved normal fault, located at the flank opposite to the weak core, develops dipping inward towards the interior of the cone (Fig. 3). In the hanging wall of this principal fault, one or several minor antithetic normal faults developed to generate a half-graben structure in a highly deformed flank. In addition, a prominent topographic bulge with up to 25 mm of positive displacement grew close to the cone base downslope of the fault system. Development of the bulge was presumably related to the development of a blind, gently dipping, inverse fault at the cone. The bulge of the edifice diameter, even for narrow weak cores (e.g., experiment H12 of Fig. 3). The location of maximum subsidence, however, located at the summit area, although extending onto the upper zone of the deformed flank (experiments H9, H11 and H15, in Fig. 3). The deformed flank develops a topographic profile with a characteristic concave–convex shape (see experiments H3, H6, H9, H12, H15, and H18 of Fig. 4), a feature which has been already suggested as indicative of flank spreading (van Wyk de Vries and Francis 1997; van Wyk de Vries and Matela 1998).

In summary, surface deformation in off-centre H-type models has a distinctive asymmetrical pattern, with intense faulting forming an asymmetrical half-graben affecting the upper-half of the flank. In addition, a prominent bulge develops near the cone base, resulting in a concave–convex shape to the cone flank (see experiments H3, H6, H9, H12, H 15, and H18 of Figs. 3 and 4).

Deformation due to the intrusion of a viscous magma body (I-type models)

Surface deformation detected at cones undergoing intrusion of a viscous magma body showed several features that were similar to those of the H-type models, including summit subsidence. However in our I-type models, deformation was different between cases where the tube intrusion is centred or off-centre with respect to the cone summit, in agreement with the results of Rincón et al. (2018). When intrusion occurred directly beneath the summit, with faulting being mainly symmetrical with two main inward-dipping normal faults forming a summit graben. In three cases, the footwall zone of one of the faults delimiting the graben also showed a small positive displacement (i.e., bulging), as in experiments I33, I35, and I41 (Fig 5). This deformation pattern is similar to that of experiments S1 and S2 (Fig. 3)

In the cases where the intrusion was below the flank (i.e., off-centre), deformation showed different pattern. This was characterised by early development of a curved normal fault perpendicular to the intruded flank and dipping inward to produce an asymmetric half-graben at the summit with up to 25 mm of subsidence at the principal fault hanging wall. The zone of maximum subsidence was thus not at the summit zone, but slightly displaced to a point above the intrusion point (see experiments I4, I18, and I40 of Fig. 5). A topographic bulge appeared in the intruded flank always at the upper-middle zone of the flank (see topographic profile of experiment I4 of Fig. 6). Therefore, this deformation pattern can be similar to that observed some of the off-centre H-type models, but in the location of the bulge is different being in the upper-middle flank for the I-type cases, and at the cone base for H-type models) (cf. experiment H12 of Fig. 4 and experiment I4 of Fig. 6).

Another characteristic deformation pattern observed in the off-centre I-type models was development of normal faults trending $\approx 30^\circ$ with respect to the first principal fault (see experiments I4 and I18 of Fig. 5). This faulting pattern developed late in the experiment, thus being a late-stage feature. Occasionally, also a “slump-like” structure also developed as a late-stage structure, defined by a U-shaped normal fault and a bulge, which formed at a highly oblique angle with regard to the initial principal fault (see experiments I4 and I40 of Fig. 5).

Discussion

Morpho-structural features indicative of potential edifice instability due to flank spreading

Our H-type experiments, simulating the gravitational deformation of a stratovolcano with a weak core of hydrothermally altered rocks, show that both centrally located (e.g., experiment

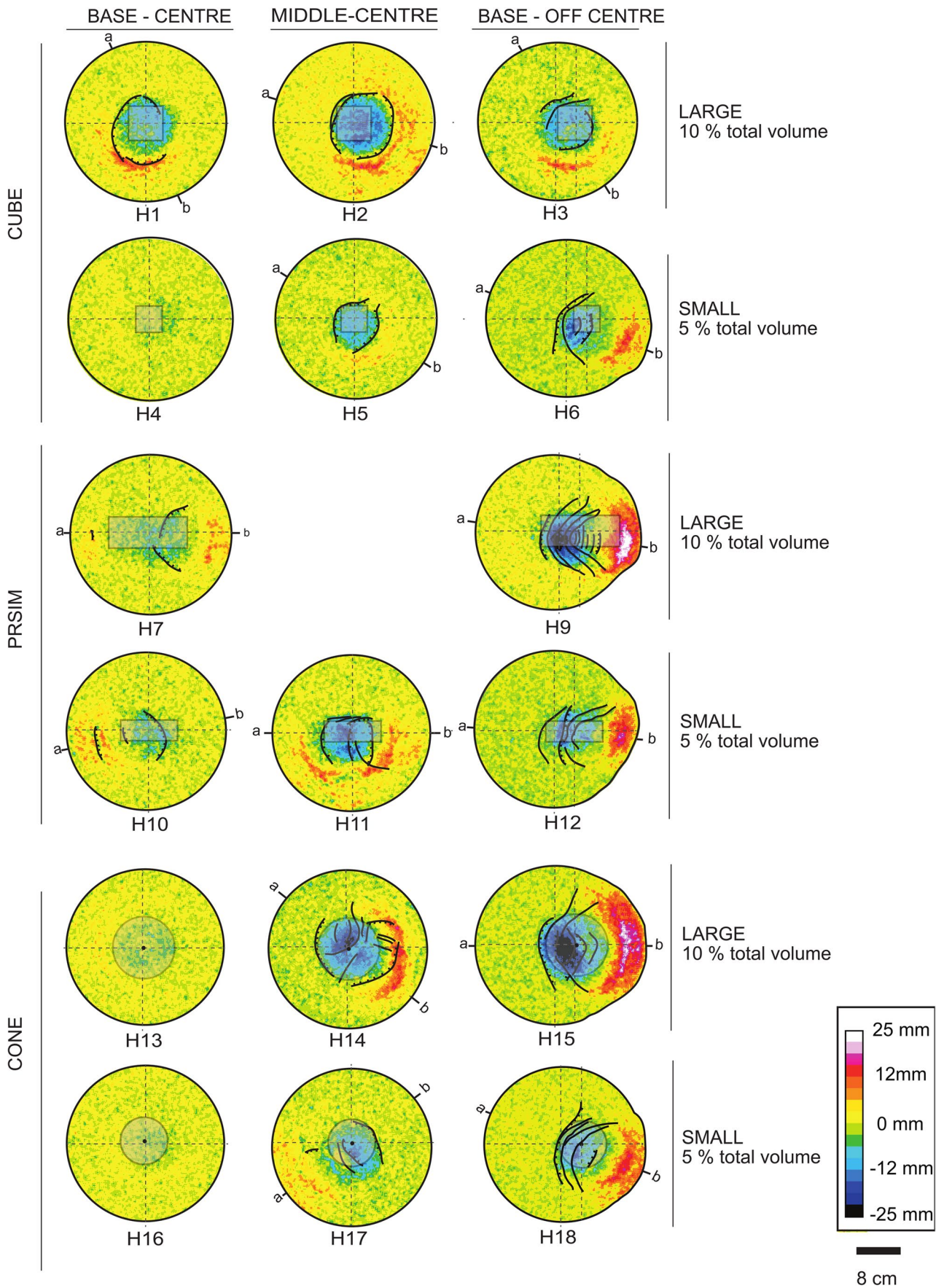


Fig. 3 Results from spreading due to the presence hydrothermal core (H-type). Variation of the distance images at time t3 (3 min in the experiment ~30,000 years in nature), with the deformation structures overlaid. Lines a–b show the location of the profiles of Fig. 4

H1 of Fig. 3) and off-centre (e.g., experiment H15 of Fig 3) hydrothermally altered zones can result in asymmetric spreading. However, the asymmetrical deformation to cause flank spreading in a preferential direction is only observed in models where the weak core is off-centre, in agreement with results

of Cecchi et al. (2004) (see Fig. 7c). Characteristic fault patterns included development of a normal principal fault (f1) which when coupled with a including a strongly deformed flank (Fig. 7c), compromises stability.

Our models show that deformation can occur even when the weak hydrothermally altered core comprise only 5% by volume of the edifice (see experiments H5, H11, and H17 of Fig. 3), showing that even quite small hydrothermal systems relative to the total volume of the edifice can potentially generate instability in stratovolcanoes. Thus, when defining

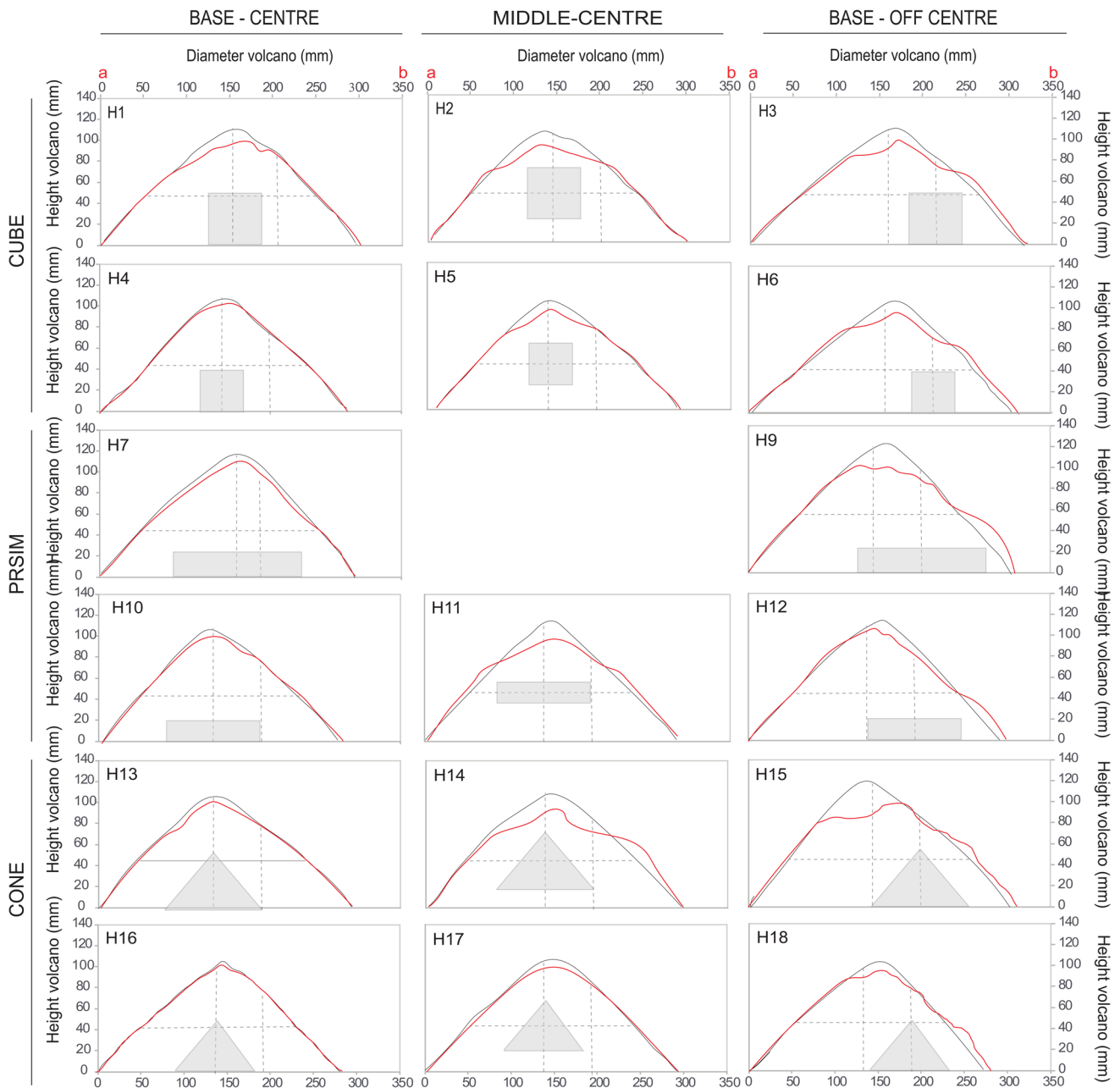


Fig. 4 Red line: topographic profiles of the H-type experiments at time t3 (3 min into the experiment, ~30,000 years for the natural system), compared with initial profiles (black line). In grey: weak-cored geometry at the start of the experiment

possible zones of weakness within a volcanic edifice, it is important to constrain the size, viscosity, and location of a hydrothermal systems within the edifice.

One of the most characteristic topographic features observed in our models of cone spreading in response to the presence of a weak core is the development of a flat (low slope) summit area due to edifice subsidence (i.e., the blue zone of Fig. 7). However, this graben-like flat area can be difficult to identify at natural systems, since subsequent lava flows from a summit vent can drape and mask topographic

scarps produced by faulting. Furthermore, since both the symmetrical (Fig. 7a) and asymmetrical (Fig. 7c) spreading of the edifice produce subsidence at the summit area, this criterion is ineffective for the identification of potential instability. Similarly, if deformation is the result of an old viscous magma body intrusion, our I-type models show that a graben-like flat area due to topographic subsidence develops also at the summit zone (see b and d of Fig. 7). The occurrence of a flat summit area is therefore also ineffective in indicating the trigger of deformation.

Fig. 5 Results from cryptodome intrusion experiments (I-type). Variation in the distance image from time t20 (20 min in the experiment ~25 days for the natural system), with deformation structures overlain. Lines a–b show the location of the profiles of Fig. 6

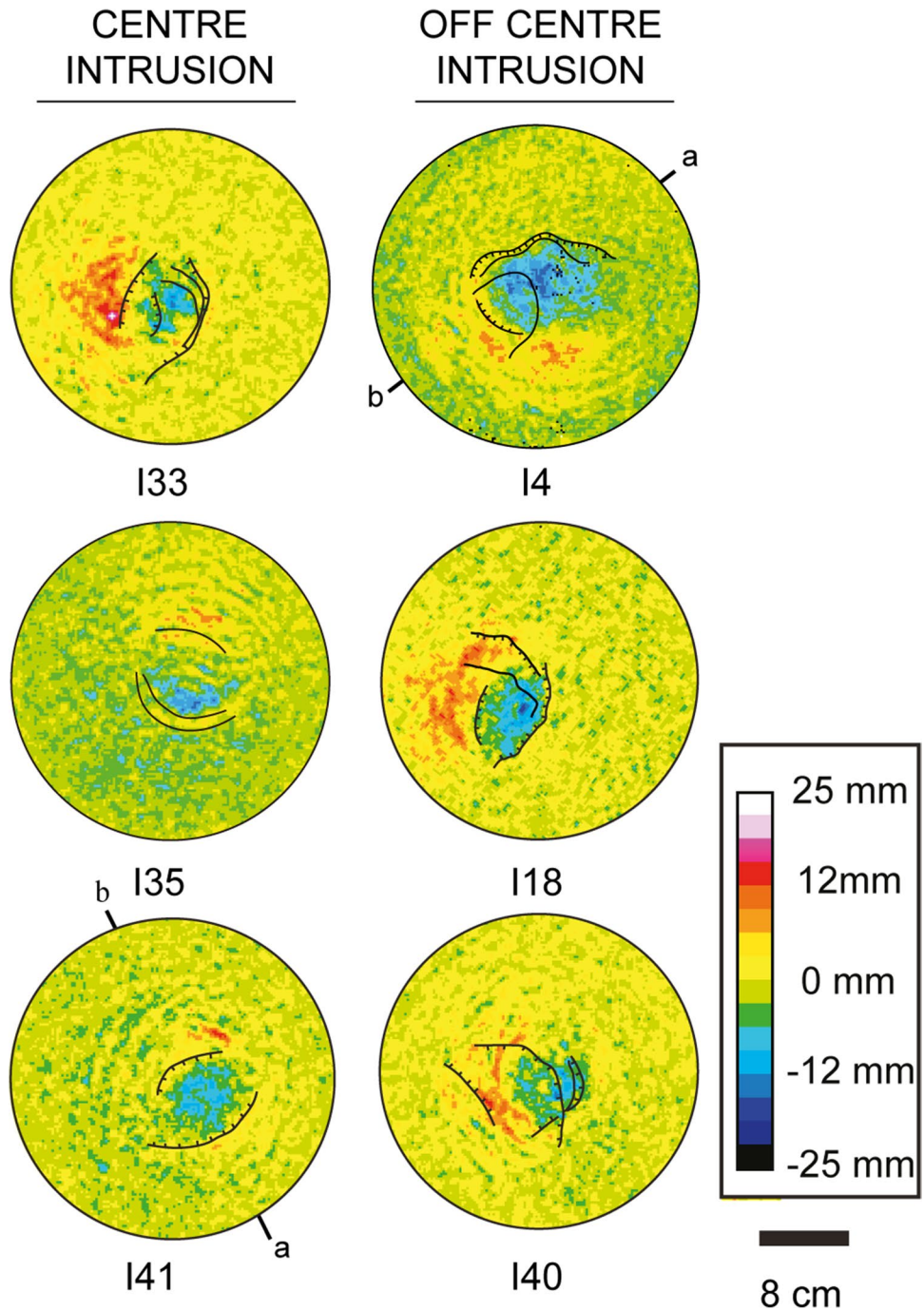


Fig. 6 Two representative examples of I-type experiments. Red line: topographic profiles at time t20 (20 min in the experiment ~25 days for the natural system) compared with initial profiles (black lines)

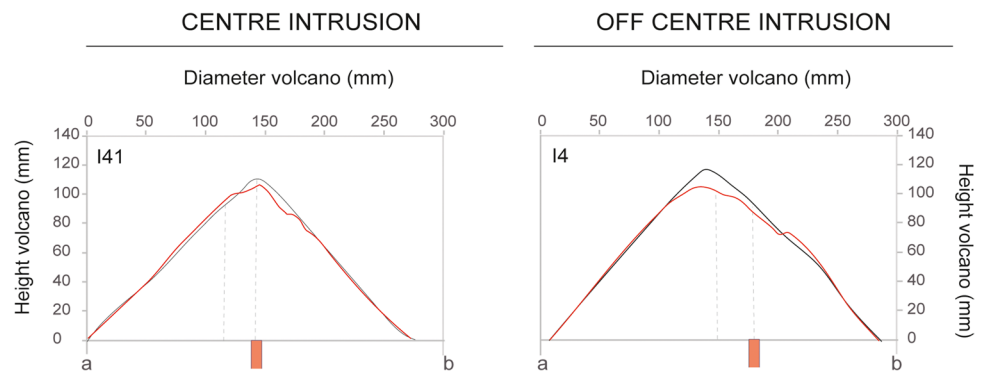
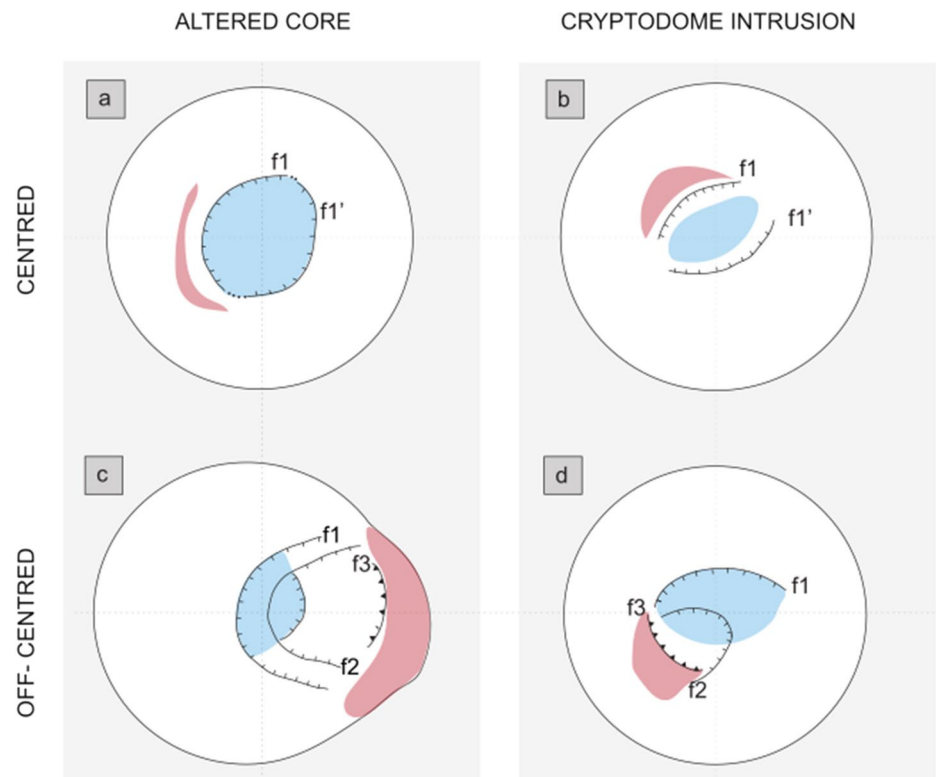


Fig. 7 Sketches of the characteristics fault patterns and topographic changes (subsidence in blue, uplift in red) revealed by (a) spreading experiments when the hydrothermal core is centre, (b) cryptodome intrusion when the tube intrusion is centre (deformation pattern 1 of Rincón et al. 2018), (c) spreading experiments when the hydrothermal core is off-centre, and (d) cryptodome intrusion when the tube intrusion is off-centre (deformation pattern 3 of Rincón et al. 2018)



Other diagnostic characteristics of deformation detected in our experiments include flank bulging. This can be detected even if later lava flows cover the area, due to both the change in slope. Donnadiou et al. (2003) compared ductile core models and intrusion models and determined that both can produce a bulge at the edifice (i.e., the red zone of Fig. 7). Their results showed that a fault-related sharp transition between subsidence and uplift was typical of intrusion-related deformation. This distinctive feature occurs in all our experiments (Fig. 6), supporting Donnadiou et al. (2003) as well as previous field observations (van Wyk de Vries et al. 2014). In addition, our I-type experiments show that deformation due to an intrusion of viscous magma located high in the edifice can result in a characteristic faulting pattern

involving development of faults with different strikes that crosscut on the upper part of the deformed flank (Fig. 7b). The presence of this faulting pattern can therefore be considered as a potential criterion for the recognition of past edifice deformation caused by an intrusion. This faulting pattern occurs in our experiments at a late stage, when the intrusion is probably located high in the edifice above the main fault plane. At this point, the edifice is therefore in a highly unstable state (Rincón et al., 2018). Thus, we propose that this faulting pattern is rarely preserved at natural system due to the likely lateral collapse that follows their formation. Thus, their scarcity in the geological record argues for the development of such a fault system as being indicative of potential collapse.

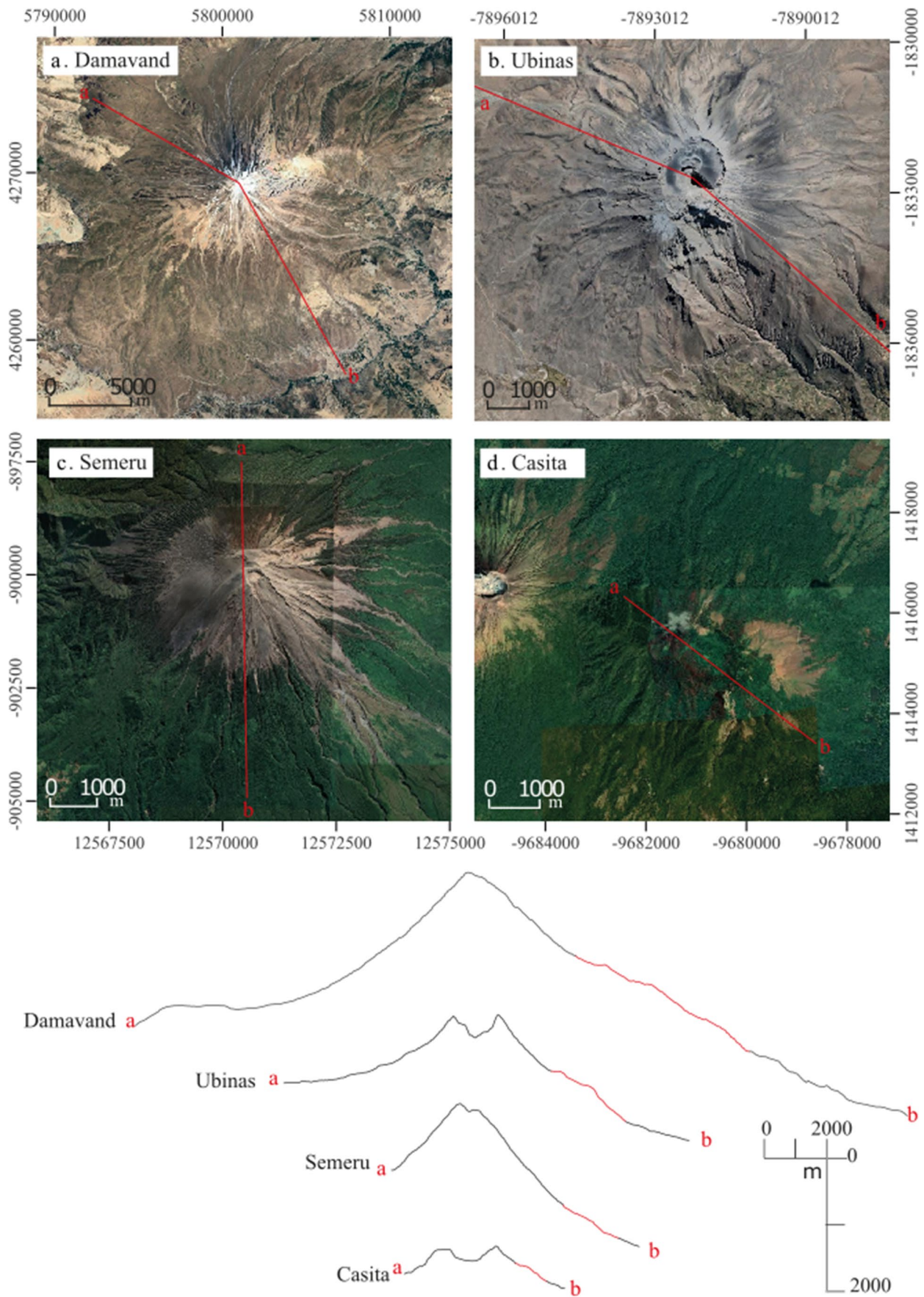


Fig. 8 Topographic profiles (from SRTM and ASTER-DEM data) of natural cases showing flank deformation potentially associated with asymmetric spreading over a weak hydrothermally altered core. Red line marks the location of the proposed flank bulge for each case

Comparative analysis of our H-type and I-type models shows that flank bulging close to the cone base only occurs in cases where the edifice is suffering from asymmetric spreading (see experiments H6, H9, H12, H15, and H18 of Figs. 3, 4 and 7c). The development of basal bulging is arises therefore a diagnostic morphological feature for the identification of asymmetric flank spreading which potentially compromises edifice stability in the sector effected.

Application to natural systems

Flank bulging, with the development of a characteristic concave–convex–concave profile on the deformed flank, has been previously proposed as a morphological criterion for identifying the development of flank spreading at several volcanoes, e.g., at Casita (van Wyk de Vries et al. 2000), Mombacho (Cecchi et al. 2004), Piton de la Fournaise (Carter et al. 2007), Teide (Márquez et al. 2008), Semeru (Solikhin et al. 2012), and Damavand (Eskandari et al. 2015). The occurrence of hydrothermally altered rocks at several of these volcanoes (including Casita, Teide, Damavand) strongly supports that flank spreading can be produced by the existence of a core of weak rocks inside the edifice. In applying our morphological criteria to these proposed examples of flank spreading some notable features appear; in some cases providing new perspectives on existing controversies regarding the role of flank spreading.

Casita (Nicaragua; 1405 m a.s.l.) is a ≈ 1000 m high dormant stratovolcano, which is part of an elongated massif including San Cristobal volcano and La Pelona caldera. Casita is not a single cone, but a $\approx 7 \times 5$ km ESE-WSW-oriented cratered ridge, formed by a series of cones and cut by sub-radial normal faults (Kerle & van Wyk de Vries 2001; van Wyk de Vries et al. 2000). Evidence for hydrothermal activity at Casita includes active fumarole fields, and this extensive hydrothermal activity has probably formed a weak core in the edifice (Van Wyk de Vries et al. 2000). Van Wyk de Vries et al. (2000) proposed that spreading is occurring on Casita's eastern flank. A topographic profile across this deformed east flank (Fig. 8d) shows strong similarities with some of our cases where spreading is due to a weak core located centrally to the cone, since the convex part is located at the middle flank (cf. experiment H14 of Fig. 4), and not at its base. Asymmetric flank spreading (preferentially to the east) at Casita could be related to the buttressing effect of San Cristobal volcano at its western flank. According to our results, the unstable east flank is potentially less prone to large and deep-seated collapse than if the weak core was

located off-centre. Instead, flank-over steeping and head scar faulting produced small landslides which can transform into small but highly mobile debris avalanches or lahars, as occurred on the SE flank in 1998 (Kerle & van Wyk de Vries 2001). The 1998 landslide left a small (≈ 1500 m wide) horseshoe scarp on the SE flank close to the deformed area (Kerle & van Wyk de Vries 2001).

Damavand volcano (Iran; 5670 m a.s.l.) is a large (400 km^3) stratovolcanoes (Eskandari et al. 2015). It is a more than 2000 m high dormant composite cone with fumarolic activity near the summit and hot springs on its flanks, located in the central Alborz Mountains ~ 50 km north of Tehran (Shirzaei et al. 2011; Eskandari et al. 2015). Despite the large difference on size, Damavand has some morphological features similar to Casita, with a characteristic concave–convex–concave-shaped SE flank (Fig. 8a), bounded to the north by a shallow horseshoe scarp. The E-SE flank is also actively deforming at a rate of several millimetres per year Shirzaei et al. (2011). This deformation is eastward and downward on the upper concave flank, and eastward in the convex zone (Shirzaei et al. 2011; see their Fig. 3). This deformation pattern is like that occurring in our models with a centre weak core, with a bulge zone locate in the middle of the flank (e.g., H14 of Fig. 3). There is topographic asymmetry between Damavand's base at the western and eastern flanks (Fig. 8a). This asymmetry could be the result of asymmetric spreading preferentially to the east. Our observations support previous suggestions by Shirzaei et al. (2011) and Eskandari et al. (2015) that Damavand's south-eastern flank can be potentially unstable due to asymmetric flank spreading. This constitutes a serious hazard and high risk, as a possible debris avalanche would impact the village of Ask and other localities in the Haraz River valley at the south-eastern foot of the volcano. The flank morphology also supports the proposal of Cecchi et al. (2004) that shallow horseshoe-shaped structures on volcano flanks can be produced by flank spreading so as to be a diagnostic feature of edifice deformation and instability.

Semeru volcano (Indonesia; 3676 m a.s.l.) is an active stratovolcano of $\approx 60 \text{ km}^3$ and ≈ 2000 m in height, located at the southern end of the Semeru–Tengger volcanic massif on Java Island (Thouret et al. 2007). Solikhin et al. (2012) proposed that the existence of a topographic bulge at the base of the SE flank is produced by thrust faults resulting from asymmetric flank spreading of the weak-cored volcano (Fig. 8c). According to our models, Semeru's stability could be strongly compromised since the location of a bulge close to the base of an edifice is indicative of deformation over an off-centre weak core. Such a case will have a fault system geometry prone to producing large deep-seated collapses (see also Fig. 9 of Solikhin et al. 2012). However, inspection of volcano slope map cast doubts over the existence of a deformation-related bulge at the edifice base, since the

change in slope defining the alleged southern bulge is quite small, discontinuous, and lobate, and does not extend across a significant part of the edifice base. This case highlights the need to analyse both the topographic profile as well as to the map distribution and extent of morphological and structural surface features so as to properly constrain, check and confirm the existences of spreading (Fig. 7).

We have also made a preliminary bibliographic survey of papers dealing with morphology, faulting patterns and geometry of hydrothermal systems at stratovolcanoes worldwide. At cases potentially suggestive of deformation due to flank spreading, we have analysed satellite images (mainly from Google Earth) and Digital Elevation Models (Shuttle Radar Topography Mission SRTM and Advanced Spaceborne Thermal Emission and Reflection Radiometer-Digital Elevation Model Aster-DEM). Our goal was the identification of other possible uncited examples of stratovolcanoes showing morphological features potentially indicative of flank spreading (i.e., concave–convex–concave flanks, possibly related to shallow horseshoe structures).

The most notable example found is Ubinas volcano (Ecuador; 5672 m a.s.l.), located in the Western Cordillera of the Andes. Ubinas is a large ($\approx 56 \text{ km}^3$) active stratovolcano and sits on the edge of a high plateau rising 1400 m above surrounding areas (Thouret et al. 2005; Rivera et al. 2010). Fumarolic activity and hydrothermal alteration occur in the summit caldera (Gonzales et al. 2014). Topographic analysis shows that a concave–convex–concave-shaped flank (with an area $\sim 2 \times 1 \text{ km}$), and bounded by a horseshoe scarp, occurs at on southeast flank (Fig. 8b). The horseshoe scarp has been attributed to the occurrence of a large sector collapse that occurred volcano around 3670 year B. P. and involving hydrothermally altered blocks (Thouret et al. 2005). Geophysical data shows that Ubinas has a well-developed hydrothermal system with a south-eastern trend and an asymmetric distribution (Gonzales et al. 2014). In fact, Ubinas is considered to be a highly unstable edifice, and the possibility of a flank failure of the hydrothermally altered zone (which is in the area of the previous collapse) is yet to be considered in the possible eruptive scenarios used for hazard assessment at this location (Thouret et al. 2005). The morphology and structure of the NE flank fit with our models where a centre weak core is located centrally the volcano edifice, since the convex part of the slope profile is located at the middle flank, and not at its base. This suggests that the area where volcano edifice stability is compromised is larger than that considered by Thouret et al. (2005), since it is not restricted to the horseshoe scarp but instead includes the entire deformed SE flank. This area is considered part of the high-hazard zone by Rivera et al. (2010), and potential lateral collapses from this unstable area, located upslope of Ubinas town, constitutes a hazard that must be considered. Previous monitoring flank deformation at Ubinas using

InSAR has not shown any signal (Rivera et al. 2010). However, we suggest that monitoring of, potential slow but long-term gravitational deformation of the SE flank is necessary due to the high risk associated with lateral collapse.

Conclusions

Our experiments show that both the existence of a hydrothermal altered weak core or intrusion of a viscous magma body can produce two different deformation patterns at stratovolcanoes, symmetric and asymmetric. Asymmetric deformation patterns can induce instability of the deformed flank producing structures that potentially induce, and can be the prelude to catastrophic collapse. We identify three morpho-structural criteria which could discriminate between asymmetric edifice deformation due to spreading. Spreading can be triggered by generation of a weak hydrothermal core or by intrusion of a viscous magma body. While a sharp transition between areas of subsidence and uplift is typical of intrusion-related deformation, the development of faults with oblique strikes crosscutting in the upper part of the deformed flank occurs only at intrusion experiments, and development of a bulge close to the cone base only occurs during asymmetric spreading. Diagnostic application of these criteria to natural cases is hampered by tendency of collapse at volcanoes deformed by off-centre viscous intrusions, which erases the characteristic late-stage faulting patterns observed in our experiments. Development of basal bulging is the main diagnostic morphological feature for the identification of asymmetric spreading, potentially compromising stability. The search for, and characterisation of, such basal bulges through remote sensing techniques or by setting up geodetic monitoring networks can provide an essential tool for hazard assessment and monitoring strategy at potentially unstable volcanoes.

Supplementary Information The online version contains supplementary material available at <https://doi.org/10.1007/s00445-023-01635-2>.

Acknowledgments We acknowledge the useful and constructive review from anonymous reviewers, and editors which have greatly improved the manuscript.

Funding Open Access funding provided thanks to the CRUE-CSIC agreement with Springer Nature. This research has been partially funded by Universidad Rey Juan Carlos (granting of funding for URJC Research Groups) and project CGL2014-58821-C2-1-R.

Open Access This article is licensed under a Creative Commons Attribution 4.0 International License, which permits use, sharing, adaptation, distribution and reproduction in any medium or format, as long as you give appropriate credit to the original author(s) and the source, provide a link to the Creative Commons licence, and indicate if changes were made. The images or other third party material in this article are included in the article's Creative Commons licence, unless indicated otherwise in a credit line to the material. If material is not included in

the article's Creative Commons licence and your intended use is not permitted by statutory regulation or exceeds the permitted use, you will need to obtain permission directly from the copyright holder. To view a copy of this licence, visit <http://creativecommons.org/licenses/by/4.0/>.

References

- Acocella V (2005) Modes of sector collapse of volcanic cones: insights from analogue experiments. *J Geophys Res* 110:B02205. <https://doi.org/10.1029/2004JB003166>
- Andrade SD, van Wyk de Vries B (2010) Structural analysis of the early stages of catastrophic stratovolcano flank-collapse using analogue models. *Bull Volcanol* 72(7):771–789. <https://doi.org/10.1007/s00445-010-0363-x>
- Belousov A, Voight B, Belousova M (2007) Directed blasts and blast-generated pyroclastic density currents: a comparison of the Bezymianny 1956, Mount St Helens 1980, and Soufrière Hills, Montserrat 1997 eruptions and deposits. *Bull Volcanol* 69(7):701–740. <https://doi.org/10.1007/s00445-006-0109-y>
- Berger BR, Henley RW (2011) Magmatic-vapor expansion and the formation of high-sulfidation gold deposits: structural controls on hydrothermal alteration and ore mineralization. *Ore Geol Rev* 39(1–2):75–90. <https://doi.org/10.1016/j.oregeorev.2010.11.003>
- Borgia A, van Wyk de Vries B (2003) The volcano-tectonic evolution of Concepción, Nicaragua. *Bull Volcanol* 65(4):248–266. <https://doi.org/10.1007/s00445-002-0256-8>
- Borgia A, Ferrari L, Pasquarè G (1992) Importance of gravitational spreading in the tectonic and volcanic evolution of Mount Etna. *Nature* 357(6375):231–235. <https://doi.org/10.1038/357231a0>
- Calvín P, Santolaria P, Román Berdiel T, Tierz P (2013) Aportaciones de la modelización analógica al estudio de la deformación intraplaca. *Geogaceta* 53:49–52
- Carrasco-Núñez G, Siebert L, Capra L (2011) Hazards from volcanic avalanches. In: Veress B, Szigethy J (eds) *Horizons in Earth Science Research 3*. Nova Science Publishers, Inc, New York, pp 199–227
- Carter A, van Wyk de Vries B, Kelfoun K, Bachèlery P, Briole P (2007) Pits, rifts and slumps: the summit structure of Piton de la Fournaise. *Bull Volcanol* 69(7):741–756. <https://doi.org/10.1007/s00445-006-0103-4>
- Cecchi E, van Wyk de Vries B, Lavest JM (2004) Flank spreading and collapse of weak-cored volcanoes. *Bull Volcanol* 67(1):72–91. <https://doi.org/10.1007/s00445-004-0369-3>
- Darmawan H, Yuliantoro P, Rakhman A, Santoso AB, Humaida H, Suryanto W (2020) Dynamic velocity and seismic characteristics of gravitational rockfalls at the Merapi lava dome. *J Volcanol Geotherm Res* 404:107010. <https://doi.org/10.1016/j.jvolgeores.2020.107010>
- Day SJ (1996) Hydrothermal pore fluid pressure and the stability of porous, permeable volcanoes. *Geol Soc London Spec Pub* 110(1):77–93. <https://doi.org/10.1144/GSL.SP.1996.110.01.06>
- Delcamp A, van Wyk de Vries B, James MR (2008) The influence of edifice slope and substrata on volcano spreading. *J Volcanol Geotherm Res* 177(4):925–943. <https://doi.org/10.1016/j.jvolgeores.2008.07.014>
- Donnadieu F, Kelfoun K, van Wyk de Vries B, Cecchi E, Merle O (2003) Digital photogrammetry as a tool in analogue modelling: applications to volcano instability. *J Volcanol Geotherm Res* 123(1–2):161–180. [https://doi.org/10.1016/S0377-0273\(03\)00034-9](https://doi.org/10.1016/S0377-0273(03)00034-9)
- Eskandari A, De Rosa R, Amini S (2015) Remote sensing of Damavand volcano (Iran) using Landsat imagery: implications for the volcano dynamics. *J Volcanol Geotherm Res* 306:41–57. <https://doi.org/10.1016/j.jvolgeores.2015.10.001>
- Gonzales K, Finizola A, Lénat JF, Macedo O, Ramos D, Thouret JC, Fournier N, Cruz V, Pistre K (2014) Asymmetrical structure, hydrothermal system and edifice stability: The case of Ubinas volcano, Peru, revealed by geophysical surveys. *J Volcanol Geotherm Res* 276:132–144. <https://doi.org/10.1016/j.jvolgeores.2014.02.020>
- Heap MJ, Baumann T, Gilg HA, Kolzenburg S, Ryan AG, Villeneuve M, Russel JK, Kennedy LA, Rosas-Carbajal M, Clynne MA (2021) Hydrothermal alteration can result in pore pressurization and volcano instability. *Geology* 49(11):1348–1352. <https://doi.org/10.1130/G49063.1>
- Horwell CJ, Williamson BJ, Llewellyn EW, Damby DE, Le Blond JS (2013) The nature and formation of cristobalite at the Soufrière Hills volcano, Montserrat: implications for the petrology and stability of silicic lava domes. *Bull Volcanol* 75(3):1–19
- Hubbert MK (1937) Theory of scale models as applied to the study of geologic structures. *Geol Soc Am Bull* 48:1459–1520. <https://doi.org/10.1130/GSAB-48-1459>
- Kelfoun K, Santoso AB, Latchimy T, Bontemps M, Nurdien I, Beauducel F et al (2021) Growth and collapse of the 2018–2019 lava dome of Merapi volcano. *Bull Volcanol* 83(2):1–13
- Kerle N, van Wyk de Vries B (2001) The 1998 debris avalanche at Casita volcano, Nicaragua—investigation of structural deformation as the cause of slope instability using remote sensing. *J Volcanol Geotherm Res* 105(1–2):49–63. [https://doi.org/10.1016/S0377-0273\(00\)00244-4](https://doi.org/10.1016/S0377-0273(00)00244-4)
- Lagmay AMF, van Wyk de Vries B, Kerle N, Pyle DM (2000) Volcano instability induced by strike-slip faulting. *Bull Volcanol* 62(4):331–346. <https://doi.org/10.1007/s004450000103>
- López DL, Williams SN (1993) Catastrophic volcanic collapse: relation to hydrothermal processes. *Science* 260(5115):1794–1796. <https://doi.org/10.1126/science.260.5115.1794>
- Márquez A, López I, Herrera R, Martín-González F, Izquierdo T, Carreno F (2008) Spreading and potential instability of Teide volcano, Tenerife Canary Islands. *Geophys Res Lett* 35(5). <https://doi.org/10.1029/2007GL032625>
- Matsunaga Y, Kanda W, Takakura S, Koyama T, Saito Z, Seki K, Suzuki A, Kishita T, Ogawa Y (2020) Magmatic hydrothermal system inferred from the resistivity structure of Kusatsu-Shirane Volcano. *J Volcanol Geotherm Res* 390:106742. <https://doi.org/10.1016/j.jvolgeores.2019.106742>
- McGuire WJ (1996) Volcano instability: a review of contemporary themes. *Geol Soc London Spec Pub* 110(1):1–23. <https://doi.org/10.1144/GSL.SP.1996.110.01.01>
- Merle O, Borgia A (1996) Scaled experiments of volcanic spreading. *J Geophys Res* 101:13,805–13,817. <https://doi.org/10.1029/95JB03736>
- Michon L, Saint-Ange F (2008) Morphology of Piton de la Fournaise basaltic shield volcano (La Réunion Island): characterization and implication in the volcano evolution. *J Geophys Res* 113(B3). <https://doi.org/10.1029/2005JB004118>
- Moore JG, Albee WC (1981) Topographic and structural change. US Geological Survey Professional Paper, p 123
- Pevear DR, Dethier DP, Frank D (1982) Clay minerals in the 1980 deposits from Mount St. Helens. *Clays Clay Miner* 30(4):241–252
- Pinkerton H, Stevenson RJ (1992) Methods of determining the rheological properties of magmas at sub-liquidus temperatures. *J Volcanol Geotherm Res* 53(1–4):47–66. [https://doi.org/10.1016/0377-0273\(92\)90073-M](https://doi.org/10.1016/0377-0273(92)90073-M)
- Reid ME (2004) Massive collapse of volcano edifices triggered by hydrothermal pressurization. *Geology* 32(5):373–376. <https://doi.org/10.1130/G20300.1>
- Reid ME, Sisson TW, Brien DL (2001) Volcano collapse promoted by hydrothermal alteration and edifice shape, Mount Rainier. *Washington Geology* 29(9):779–782. [https://doi.org/10.1130/0091-7613\(2001\)029<0779:VCPBHA>2.0.CO;2](https://doi.org/10.1130/0091-7613(2001)029<0779:VCPBHA>2.0.CO;2)
- Rincón M (2019) Evaluación de la deformación e inestabilidad de edificios volcánicos por procesos de intrusión mediante análogos. PhD thesis,. Rey Juan Carlos University, Madrid, Spain <https://hdl.handle.net/10115/17538>

- Rincón M, Márquez A, van Wyk de Vries B, Herrera R, Bruña JLG, Llanes P (2015) Aplicación del sensor Kinect en modelos análogos para la identificación morfo-estructural de procesos de deformación en volcanes. *Geogaceta* 57:107–110
- Rincón M, Márquez A, Herrera R, Alonso-Torres A, Granja-Bruña JL, van Wyk de Vries B (2018) Contrasting catastrophic eruptions predicted by different intrusion and collapse scenarios. *Sci Rep* 8(1):1–11. <https://doi.org/10.1038/s41598-018-24623-5>
- Rincón M, Márquez A, Herrera R, Galland O, Sánchez-Oro J, Concha D, Montemayor AS (2022) Monitoring volcanic and tectonic sandbox analogue models using the Kinect v2 sensor. *Earth Space Sci* 9(6):e2020EA001368. <https://doi.org/10.1029/2020EA001368>
- Rivera M, Thouret JC, Mariño J, Berolatti R, Fuentes J (2010) Characteristics and management of the 2006–2008 volcanic crisis at the Ubinas volcano (Peru). *J Volcanol Geotherm Res* 198(1–2):19–34. <https://doi.org/10.1016/j.jvolgeores.2010.07.020>
- Rosas-Carbajal M, Komorowski JC, Nicollin F, Gibert D (2016) Volcano electrical tomography unveils edifice collapse hazard linked to hydrothermal system structure and dynamics. *Sci Rep* 6(1):1–11. <https://doi.org/10.1038/srep29899>
- Salaün A, Villemant B, Gérard M, Komorowski JC, Michel A (2011) Hydrothermal alteration in andesitic volcanoes: trace element redistribution in active and ancient hydrothermal systems of Guadeloupe (Lesser Antilles). *J Geochem Explor* 111(3):59–83. <https://doi.org/10.1016/j.gexplo.2011.06.004>
- Samaniego P, Valderrama P, Mariño J, van Wyk de Vries B, Roche O, Manrique N, Chédeville C, Liorzou C, Fidel L, Malnati J (2015) The historical (218 ± 14 aBP) explosive eruption of Tutupaca volcano (Southern Peru). *Bull Volcanol* 77(6):1–18. <https://doi.org/10.1007/s00445-015-0937-8>
- Seisedos J, Ferrer M, de Vallejo LG (2012) Geological and geomechanical models of the pre-landslide volcanic edifice of Güímar and La Orotava mega-landslides (Tenerife). *J Volcanol Geotherm Res* 239:92–110. <https://doi.org/10.1016/j.jvolgeores.2012.06.013>
- Sekiya S, Kikuchi Y (1890) The eruption of Bandai-san. *J Coll Sci, Imperial University, Japan* 3:91–172
- Shirzaei M, Walter TR, Nankali HR, Holohan EP (2011) Gravity-driven deformation of Damavand volcano, Iran, detected through InSAR time series. *Geology* 39(3):251–254. <https://doi.org/10.1130/G31779.1>
- Siebert L (1992) Threats from debris avalanches. *Nature* 356:658–659. <https://doi.org/10.1038/356658a0>
- Siebert L, Glicken H, Ui T (1987) Volcanic hazards from Bezymianny- and Bandai-type eruptions. *Bull Volcanol* 49(1):435–459. <https://doi.org/10.1007/BF01046635>
- Solikhin A, Thouret JC, Gupta A, Harris AJ, Liew SC (2012) Geology, tectonics, and the 2002–2003 eruption of the Semeru volcano, Indonesia: Interpreted from high-spatial resolution satellite imagery. *Geomorphology* 138(1):364–379. <https://doi.org/10.1016/j.geomorph.2011.10.001>
- Takahashi K, Takakura S, Matsushima N, Fujii I (2018) Relationship between volcanic activity and shallow hydrothermal system at Meakandake volcano, Japan, inferred from geomagnetic and audio-frequency magnetotelluric measurements. *J Volcanol Geotherm Res* 349:351–369. <https://doi.org/10.1016/j.jvolgeores.2017.11.019>
- Thouret JC, Rivera M, Wörner G, Gerbe MC, Finizola A, Fornari M, Gonzales K (2005) Ubinas: the evolution of the historically most active volcano in southern Peru. *Bull Volcanol* 67(6):557–589. <https://doi.org/10.1007/s00445-004-0396-0>
- Thouret JC, Lavigne F, Suwa H, Sukatja B (2007) Volcanic hazards at Mount Semeru, East Java (Indonesia), with emphasis on lahars. *Bull Volcanol* 70:221–244. <https://doi.org/10.1007/s00445-007-0133-6>
- Tibaldi A, Bistacchi A, Pasquare FA, Vezzoli L (2006) Extensional tectonics and volcano lateral collapses: insights from Ollagüe volcano (Chile-Bolivia) and analogue modelling. *Terra Nova* 18(4):282–289. <https://doi.org/10.1111/j.1365-3121.2006.00691.x>
- Tibaldi A, Corazzato C, Kozhurin A, Lagmay AFM, Pasquaré Mariotto F, Ponomareva V, Rust D, Tormey D, Vezzoli L (2008) Influence of substrate tectonic heritage on the evolution of composite volcanoes: predicting sites of flank eruption, lateral collapse, and erosion. *Glob Planet Change* 61(3–4):151–174. <https://doi.org/10.1016/j.gloplacha.2007.08.014>
- Tortini R, Bonali FL, Corazzato C, Carn SA, Tibaldi A (2014) An innovative application of the Kinect in Earth sciences: quantifying deformation in analogue modelling of volcanoes. *Terra Nova* 26(4):273–281. <https://doi.org/10.1111/ter.12096>
- van Wyk de Vries B, Francis PW (1997) Catastrophic collapse at stratovolcanoes induced by gradual volcano spreading. *Nature* 387(6631):387–390. <https://doi.org/10.1038/387387a0>
- van Wyk de Vries B, Matela R (1998) Styles of volcano-induced deformation: numerical models of substratum flexure, spreading and extrusion. *J Volcanol Geotherm Res* 81:1–18. [https://doi.org/10.1016/S0377-0273\(97\)00076-0](https://doi.org/10.1016/S0377-0273(97)00076-0)
- van Wyk de Vries B, van Wyk de Vries M (2018) Tectonics and volcanic and igneous plumbing systems. In: Burchardt (ed) *Volcanic and igneous plumbing systems: understanding magma transport, storage, and evolution in the Earth's crust*. Elsevier, Uppsala, pp 167–189. <https://doi.org/10.1016/B978-0-12-809749-6.00007-8>
- van Wyk de Vries B, Kerle N, Petley D (2000) Sector collapse forming at Casita volcano, Nicaragua. *Geology* 28(2):167–170. [https://doi.org/10.1130/0091-7613\(2000\)28<167:SCFACV>2.0.CO;2](https://doi.org/10.1130/0091-7613(2000)28<167:SCFACV>2.0.CO;2)
- van Wyk de Vries B, Márquez A, Herrera R, Bruña JL, Llanes P, Delcamp A (2014) Craters of elevation revisited: forced-folds, bulging and uplift of volcanoes. *Bull Volcanol* 76(11):1–20. <https://doi.org/10.1007/s00445-014-0875-x>
- Voight B, Janda RJ, Glicken H, Douglass PM (1983) Nature and mechanics of the Mount St Helens rockslide-avalanche of 18 May 1980. *Geotechnique* 33(3):243–273. <https://doi.org/10.1680/geot.1983.33.3.243>
- Voight B, Komorowski JC, Norton GE, Belousov AB, Belousova M, Boudon G, Francis PW, Franz W, Heinrich P, Sparks RSJ, Young SR (2002) The 26 December (Boxing Day) 1997 sector collapse and debris avalanche at Soufriere Hills volcano, Montserrat. *Geol Soc Lond Mem* 21(1):363–407. <https://doi.org/10.1144/GSL.MEM.2002.021.01.17>
- Zimbelman D, Watters RJ, Bowman S, Firth I (2003) Quantifying hazard and risk assessments at active volcanoes. *Eos, Transactions AGU* 84(23):213–217. <https://doi.org/10.1029/2003EO230001>